Biometals (2012) 25:203–217
DOI 10.1007/s10534-011-9498-2

Iron-induced remodeling in cultured rat pulmonary artery endothelial cells

Nikolai V. Gorbunov · James L. Atkins · Narasimman Gurusamy · Bruce R. Pitt

Received: 24 December 2010 / Accepted: 22 September 2011

Abstract Although iron is known to be a component of the pathogenesis and/or maintenance of acute lung injury (ALI) in experimental animals and human subjects, the majority of these studies have focused on disturbances in iron homeostasis in the airways resulting from exposure to noxious gases and particles. Considerably less is known about the effect of increased plasma levels of redox-reactive non-transferrin bound iron (NTBI) and its impact on pulmonary endothelium. Plasma levels of NTBI can increase under various pathophysiological conditions, including those associated with ALI, and multiple mechanisms are in place to affect the [Fe^{2+}]/[Fe^{3+}] redox steady state. It is well accepted, however, that intracellular transport of NTBI occurs after reduction of [Fe^{3+}] to [Fe^{2+}] (and is mediated by divalent metal transporters). Accordingly, as an experimental model to investigate mechanisms mediating vascular effects of redox reactive iron, rat pulmonary artery endothelial cells (RPAECs) were subjected to pulse treatment (10 min) with [Fe^{2+}] nitriloacetate (30 μM) in the presence of pyrithione, an iron ionophore, to acutely increase intracellular labile pool of iron. Cellular iron influx and cell shape profile were monitored with time-lapse imaging techniques. Exposure of RPAECs to [Fe^{2+}] resulted in: (i) an increase in intracellular iron as detected by the iron sensitive fluorophore, PhenGreen; (ii) depletion of cell glutathione; and (iii) nuclear translocation of stress-response transcriptional factors Nrf2 and NFkB (p65). The resulting iron-induced cell alterations were characterized by cell polarization and formation of membrane cuplike and microvilli-like projections abundant with ICAM-1, caveolin-1, and F-actin. The iron-induced re-arrangements in cytoskeleton, alterations in focal cell–cell interactions, and cell buckling were accompanied by decrease in

---

Gorbunov NV and Atkins JL equally contributed to this study.

N. V. Gorbunov
The Henry Jackson Foundation for the Advancement
of Military Medicine, Inc, Washington, DC, USA

N. V. Gorbunov · B. R. Pitt
Department of Environmental and Occupational Health,
University of Pittsburgh, Graduate School Public Health,
Pittsburgh, PA 15219, USA

N. V. Gorbunov · J. L. Atkins
Walter Reed Army Institute of Research, 503 Robert
Grant Ave, Silver Spring, MD 20910, USA

N. V. Gorbunov (✉)
8901 Wisconsin Avenue, Bethesda, MD 20889-5603,
USA
e-mail: Nikolaiv.gorbunov@gmx.us

N. Gurusamy
Cardiovascular Research Center, University
of Connecticut School of Medicine, 263 Farmington
Avenue, Farmington, CT 06030, USA

electrical resistance of RPAEC monolayer. These effects were partially eliminated in the presence of N,N′-bis (2-hydroxybenzyl) ethylenediamine-N,N′-diacetic acid, an iron chelator, and Y27632, a Rho—kinase inhibitor. Thus acute increases in labile iron in cultured pulmonary endothelium result in structural remodeling (and a proinflammatory phenotype) that occurs via post-transcriptional mechanisms regulated in a redox sensitive fashion.

Keywords Iron complexes · Endothelial cells · Remodeling · Inflammation · Redox-stress

Abbreviations

LKC	Leukocytes
EC	Endothelial cells
TEM	Transendotelial migration (i.e., diapedesis)
OS	Oxidative stress
CAM	Cell adhesion molecule
VE-cadherin	Vascular endothelial cadherin-5 (CD144)
ICAM-1	Intercellular adhesion molecule 1
Nrf2	Nuclear factor E2-related factor 2 (Keap1/Nrf2)
Ref-1	Redox factor-1
NFκB (p65)	Nuclear factor κB, subunit p65
$[Fe^{2+}]$NTA	Iron (ferrous) nitriloacetate
HBED	N,N′-bis (2-hydroxybenzyl) ethylenediamine-N,N′-diacetic acid
GSH	Glutathione

Introduction

Iron has been shown to be a component of the pathogenesis and/or maintenance of acute lung injury (ALI) in experimental animals and human subjects (Lagan et al. 2008). The majority of these studies have focused on disturbances in iron homeostasis in the airways resulting from exposure to noxious gases and particles (Turi et al. 2004). Under these conditions iron mobilization, decompartmentalization, and delocalization can lead to pathological increases in low-molecular mass complexes of iron that in turn leads to the uncontrolled formation of damaging free radicals or enhances availability of iron for a variety of invading microbes for which iron is a requisite nutrient and virulence factor. Alternatively, plasma and tissue fluid concentrations of redox-reactive chelatable, i.e., non-transferrin bound, iron can increase in conditions associated with ALI including blunt trauma, massive blood transfusion, or hemorrhage followed by transfusion of resuscitative fluids (Gorbunov et al. 2007; Esposito et al. 2003; Scheiber-Mojdehkar et al. 2004; Atkins et al. 2011). Using models of acute lung trauma, we previously demonstrated that administration of an iron chelator can decrease plasma level of chelatable iron, facilitate its excretion with urine, and moderate redox and pro-inflammatory responses in pulmonary vascular endothelium (Gorbunov et al. 2006, 2007). This study provided biochemical and morphological measures that highlighted the importance of iron-dependent redox signaling in spatial coordination of lung cell adhesion molecules (CAM) and complex changes in pulmonary endothelium and phagocytic leukocytes (LKC) accompanying acute lung inflammation. We concluded that our observations were in concert with recent models of LKC diapedesis introduced to specify mechanism of ALI (Barreiro et al. 2002; Carman and Springer 2004; Dejana 2006).

In the current study, we sought to further define structural re-arrangements and pro-inflammatory remodeling promoted by $[Fe^{2+}]$-dependent redox signaling and hence, we used a rudimentary model of cultured rat pulmonary artery endothelial cells (RPAEC) subjected to pulse (10 min) of 30 μM $[Fe^{2+}]$ complex with nitriloacetate with the ionophore, pyrithione. The resulting iron-induced cell alterations were characterized by cell polarization, formation of membrane rafts, cuplike and microvilli-like structures abundant with ICAM-1, caveolin-1, and F-actin. The associated rearrangements in cytoskeleton and cell construction were accompanied by decrease in transendothelial electric resistance. The influx of $[Fe^{2+}]$ into the cells resulted in depletion of cellular thiols and nuclear translocation of redox-sensitive transcriptional factors Nrf2 and NFkB (p65). These observed effects were sensitive to N,N′-bis (2-hydroxybenzyl) ethylenediamine-N,N′-diacetic acid (HBED), an iron chelator and antioxidant, and Y27632, a Rho—kinase inhibitor. We propose that iron-induced remodeling in RPAECs proceeds via post-transcriptional mechanisms activated in redox-dependent manner.

Materials and methods

Cell culture

Primary culture of RPAEC were a gift from Dr. Troy Stevens (University South Alabama) and cultured as described previously (Zhang et al. 2006). Cells were grown under 5% CO_2 in the MCDB-131 Complete medium (VEC Technologies, Inc.) in 75 cm^2 cell culture flasks (CORNING Inc.) and harvested upon confluence (4×10^6 cell/flask). The harvested cells were re-suspended in MCDB-131 medium, seeded on chambered slides (8 chamber/slide) with 1×10^5 cell/well, or on Delta TPG dishes (Fisher Scientific) with 3×10^5 cell/well, or on transwell filters (Costar; 12 mm diameter, 0.4 µm pore size) with 5×10^4 cell/well, and cultivated until confluence. RPAEC were incubated with sterile solutions of either 30 µM $[Fe^{2+}]$–nitriloacetate ($[Fe^{2+}]$NTA) or of 30 µM $[Fe^{2+}]$–N,N′-bis (2-hydroxybenzyl) ethylenediamine-N,N′-diacetate ($[Fe^{2+}]$HBED) in Hank's Balanced Salt Solution (HBSS, GIBCO/In Vitrogen Inc.) for 10 min in the presence of 10 µM pyrithione, a $[Fe^{2+}]$ ionophore (Kress et al. 2002; Quadri et al. 2003). For inhibition of Rho-kinase, confluent cell cultures were pre-incubated with 10 µM (R)-(+)-*trans*-N-(4-Pyridyl)-4-(1-amino-ethyl)-cyclohexanecarboxamide (Y-27632) (Calbiochem; www.emdbiosciences.com). After incubation with iron complexes, cells were either subjected to analysis for depletion of GSH or were further incubated with MCDB-131 complete medium for 2 h to assess cell redox-dependent signaling response, re-arrangements of ICAM-1 adhesion molecules, caveolin-1, and cytoskeleton, or relative electrical resistance of endothelial monolayer (REREM). Cell viability was assessed by trypan blue exclusion (necrosis) or terminal deoxynucleotidyl *trans*-ferase biotin–dUTP nick-end labelling (TUNEL) (Upstate/Millipore; www.Millipore.com) using fixed cells and/or Annexin V staining (apoptosis).

Relative electrical resistance of endothelial monolayer

For assessment of alterations of RPAEC barrier integrity, we determined REREM of cells grown on sterile BD BioCoat™ Fibrillar Collagen 1.0 µm PET Membrane 12-well cell culture inserts (BD Biosciences, Franklin Lakes, NJ). The filters were used in ENDOHM-12 chamber (World Precision Instruments, Sarasota, FL) 4 days after the cells were plated when REREM reached a base line (~28 Ω/cm^2). After a 30-min adaptation of the cells in PBS, experimental solutions were added and REREM was recorded every 10 min using EVOM Voltohmmeter (World Precision Instruments, Sarasota, FL) at 37 C (Quadri et al. 2003). The data were corrected for the resistance of the insert filters alone.

Preparation of cytosolic and nuclear extracts

The harvested cells (4×10^6 cell) were homogenized in 0.5 ml buffer A (20 mM Hepes, pH 7.9, 20% glycerol, 10 mM NaCl, 1.5 mM $MgCl_2$, 0.2 mM EDTA, 1 mM DTT, 0.1% Triton X-100, and protease inhibitors (PMSF, leupeptin, aprotinin, and pepstatin) in a Polytron homogenizer). Homogenates were centrifuged at 3,000 rpm at 4°C for 15 min and the nuclear pellet was resuspended in 5 vol of buffer B that was essentially the same as buffer A except containing 500 mM NaCl. Supernatant from the above centrifugation was further centrifuged at 10,000 rpm at 4°C for 20 min, and the resultant supernatant was used as cytosolic extract. The nuclei were lysed by incubation for 1 h on ice with intermittent tapping. Homogenates were then centrifuged at 10,000 rpm at 4°C for 15 min, and the supernatant was used as nuclear lysate. Cytosolic and nuclear extracts were aliquoted, snap-frozen, and stored at −80°C till use. Total protein concentration in both cytosolic and nuclear extract was determined using the BCA Protein assay kit (Pierce, Rockford, IL). Cytosolic and nuclear extracts were analyzed by Western-immunoblotting.

Immunoprecipitation

Nuclear extract containing 500 µg of total protein was immunoprecipitated with either anti-Nrf-2, or anti-NFκB (p65) subunit antibody (Santa Cruz Biotechnology, Inc., Santa Cruz, CA), or anti-phospho-p38 MAP kinase (Thr180/Tyr182) (Cell Signaling Technology Inc., Beverly, MA) and protein A sepharose beads (Zymed, San Francisco, CA) for overnight at 4°C. Pellets were collected by centrifuging at 10,000×*g* for 30 s at 4°C, and washed 3 times with ice-cold wash buffer (50 mM Tris–HCl, pH 7.4, 150 mM NaCl, 1% NP-40, 0.5% sodium deoxycholate, 0.1% SDS, and 2 mM EDTA). Pellets were resuspended in 1× Laemmli sample buffer, boiled at

95–100°C for 10 min, and Western immunoblotting was done as described below.

Immunoblot analysis

Proteins of cytosolic and nuclear fractions, as well as the immunoprecipitated pellet were separated in SDS-PAGE and transferred to nitrocellulose filters. Filters were blocked in 5% nonfat dry milk and probed with primary antibody for overnight. Primary antibodies against p65 subunit of NFκB, Nrf-2, phospho-p38 MAPK, glyceraldehyde-6-phosphate dehydrogenase (GAPDH) (Santa Cruz Biotechnology Inc., Santa Cruz, CA), and histone H3 (Cell Signaling Technology, Inc., Beverly, MA) were used at the dilution of 1:1,000. Protein bands were identified with horseradish peroxidase-conjugated secondary antibody (1:2,000 dilution) and Western Blotting Luminol Reagent (Cruz Biotechnology, Inc., Santa Cruz, CA). GAPDH and histone served as loading controls for cytosolic and nuclear extracts, respectively.

Cell microscopy imaging techniques and image analysis

For live cell experiments RPAEC were grown in Delta TPG dishes (Fisher Scientific) and incubated with [Fe^{2+}] complexes as described above using a modified protocol by Kress et al. 2002. Cell response to [Fe^{2+}] exposure was assessed with DIC time-lapse imaging techniques. Cell [Fe^{2+}] influx was probed in the presence of 5 μM Phen Green diacetate, a green fluorescent [Fe^{2+}] indicator (Invitrogen, Carlsbad, CA) (http://products.invitrogen.com/ivgn/en/US/). Time-lapse cell imaging was conducted with Nikon Eclipse TE 2000. Image acquisition, processing, and analysis was conducted with MetaMorph Imaging Series 5.0 software. Cell images were recorded each 15 s during 30 min observation periods.

For immunofluorescence confocal imaging cells exposed to iron complexes were fixed at 2 h following treatment and specimens were processed as described previously (Gorbunov et al. 2007). Primary antibody against ICAM-1, caveolin-1, *pho*-caveolin-1, pho-caldesmon (Santa Cruz Biotechnology Inc., Santa Cruz, CA), F-actin (Abcam Inc. Cambridge, MA), and *pho*-p38 MAPK (Cell Signaling Technology, Inc., Beverly, MA) were used with optimal dilution of 1:250. This was followed by incubation with secondary fluorochrome-conjugated antibody and nuclei counterstaining with Hoechst 33342 (Molecular Probes, Inc., Eugene OR) diluted 1:3,000. The secondary antibodies used were (i) ALEXA 488-conjugated goat anti-rabbit IgG (Molecular Probes Inc.), (ii) Cy3-conjugated donkey anti-mouse IgG (Rockland Inc., Gilbertsville, PA), negative controls for nonspecific binding included normal goat and donkey serum without primary antibody or with secondary antibody alone. The labeled specimens were rinsed, mounted in Gelvatol (Monsanto Corp., St. Louis, MO), and placed under a coverslip for fluorescence microscopy. Fluorescence microscopy of the specimens was done with a 100 × 1.4 n.a. objective lens on a Nikon Eclipse E800/Bio-Rad Radiance 2100 confocal microscope with 0.5-μm scanning Z step size. The background fluorescence was determined for each of the analyzed images of the immunolabeled proteins using images from specimens labeled with secondary antibodies only. Processing and analysis of digital images, including projections of co-localized proteins in cells (region of interest, ROI), were conducted using Simple PCI High Performance Imaging software (Compix Inc., Hamamatsu Co., http://www.cimaging.net) and image software (http://rsb.info.nih.gov). The results of imaging were verified and confirmed in independent assessment using Leica TCS SP5 confocal system with LAS AF software (Leica Microsystems Inc.).

Fluorescence assay of GSH and protein sulfhydryls

GSH concentration in RPAEC was determined using ThioGlo-1 (Covalent, Wobum, MA) a maleimide reagent that produces a highly fluorescent product upon its reaction with SH groups. GSH content was estimated by an immediate fluorescence response registered upon addition of Thio Glo-1 to the cell homogenate (Shvedova et al. 2000). Protein sulfhydryls were determined as an additional increase in fluorescence response after addition of sodium dodecyl sulfate (4.0 mM) to the same cell homogenate. A standard curve was established by the addition of GSH (0.04–4.0 μM) to 100 mM phosphate buffer, pH 7.4 containing 10 μM ThioGlo-1. Shimadzu RF-5301PC spectrofluorophotometer (Kyoto, Japan) was employed for the assay of fluorescence using excitation at 388 nm and emission at 500 nm. The data obtained were exported and treated using RF-5301PC Personal Fluorescence Software (Shimadzu).

Phospho p38 MAP kinase ELISA assay

Rat pulmonary artery endothelial cells (2×10^6 cells) were lysed in 0.2 ml of a buffer as described above. Homogenates were centrifuged at 3,000 rpm at 4°C for 15 min and the collected supernatants were subjected to the phosphor p38 MAP kinase (Thr180/Tyr182) ELISA assay (Cell Signaling Technology, Inc., Beverly, MA) using a 96-well plate coated with p38 MAP kinase antibody. After incubation with cell lysates, p38 MAP kinase protein is captured by the coated antibody. Following extensive washing, phospho-p38 MAPK (Thr180/Tyr182) mouse mAb were added to detect the captured phospho-p38 MAPK protein. HRP-linked anti-mouse antibody were then used to recognize the bound detection antibody. HRP substrate, TMB, was added to develop color. The magnitude of absorbance for this developed color was proportional to the quantity of phospho-p38 MAP kinase (Thr180/Tyr182) protein. The absorbance values were determined using the SpectraMax Plus plate reader (Molecular Devices Sunnyvale, CA).

Results

Assessment of [Fe^{2+}] influx in RPAEC challenged with [Fe^{2+}]NTA was done using fluorescence time-lapse imaging technique and PhenGreen SK (PGSK), a [Fe^{2+}]-sensitive fluorophore (Fig. 1). The cells incubated with 5 μM PGSK displayed bright green fluorescence (Fig. 1a). Challenge of the cells with 30 μM [Fe^{2+}]NTA in the presence of 10 μM pyrithione resulted in quenching of PGSK fluorescence indicating a relative increase in intracellular [Fe^{2+}] (Fig. 1b). This effect was inhibited by 50 μM TPEN, a membrane-permeant metal chelator (Fig. 1c).

Redox alterations and stress-response to challenge of RPAEC with [Fe^{2+}]. Assessment of cell GSH was used to determine cell redox alterations induced by [Fe^{2+}] influx. As shown in Fig. 2, 10 min pulse with [Fe^{2+}]NTA resulted in a decrease in GSH levels from 18.7 ± 0.4 nmol/mg (sham treatment) to 16.8 ± 0.4 nmol/mg ($P < 0.04$, $n = 6$ Dunnett's test). This effect was eliminated in the presence of HBED (Fig. 2). The observed redox stress was accompanied by nuclear translocation of stress-sensitive transcriptional factors Nrf2 and NFκB (p65) (Fig. 3). Note ten minutes exposure of the cells to 30 μM [Fe^{2+}]NTA in the presence of 10 μM pyrithione did not significantly change their viability.

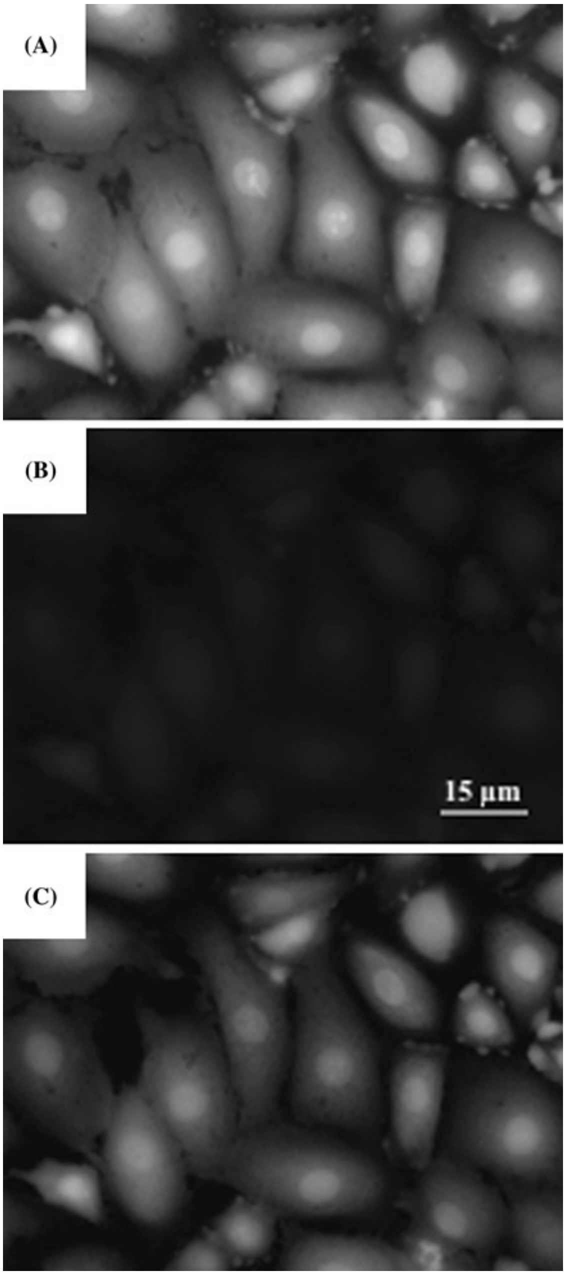

Fig. 1 Assessment of [Fe^{2+}] influx in RPAEC challenged with [Fe^{2+}]NTA in the presence of the fluorophore PhenGreen SK (PGSK). **a** Fluorescence of PGSK in RPAEC in the absence of [Fe^{2+}]NTA and pyrithione. **b** Decrease of the PGSC fluorescence at 30 s following a challenge with 30 μM [Fe^{2+}]NTA in the presence of 10 μM pyrithione. The same as "b" at 30 s after supplementation of 50 μM TPEN, a [Fe^{2+}] chelator

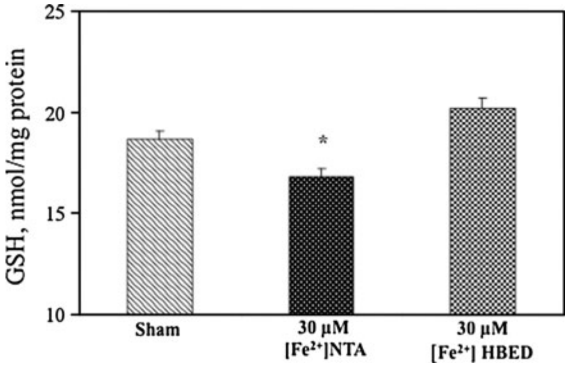

Fig. 2 Assessment of glutathione (GSH) of RPAEC challenged with [Fe^{2+}]. GSH measurement was conducted with ThioGlo-1 probe as described in "Materials and methods".$^*P < 0.04$ versus sham treatment ($n = 6$, Dunnett's test)

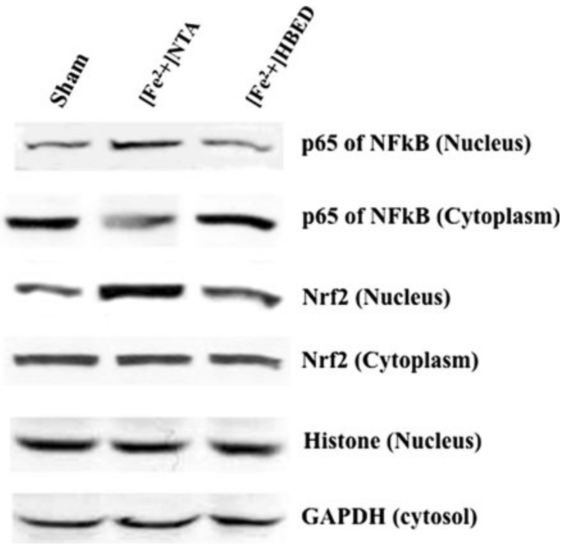

Fig. 3 Stress-response to challenge of RPAEC with [Fe^{2+}]. Immunoblot assessment of nuclear translocation of transcriptional factors Nrf2 and NFκB

These data corroborate a recent concept on crucial role of Nrf2 and NFκB (p65) in adaptive response to oxidative and electrophilic stresses, and regulation of cell iron homeostasis (Kobayashi et al. 2006; Harada et al. 2011).

The iron-induced oxidative stress has been described recently as one of the causes of increase of vascular permeability in lung (Gorbunov et al. 2007). Therefore, the next set of experiments was focused on assessment of structural integrity of RPAEC monolayers challenged with [Fe^{2+}] complexes.

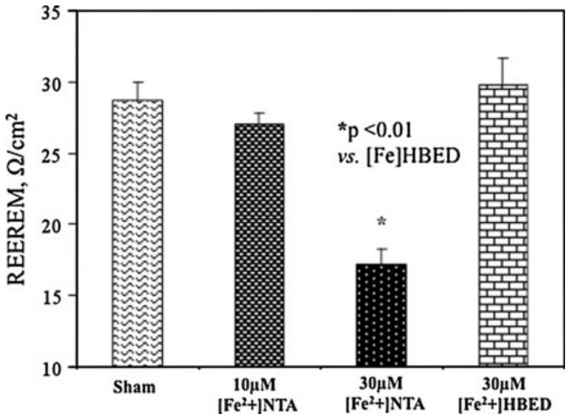

Fig. 4 Assessment of relative electrical resistance of RPAEC monolayers challenged with [Fe^{2+}]. RPAEC in PBS + 10 µM pyrithione (sham treatment) were exposed to 30 µM [Fe^{2+}]NTA or 30 µM [Fe^{2+}]HBED solutions for 10 min at 37°C then incubation solutions were replaced with fresh PBS. Assessment of REREM was done as described in "Materials and methods". The monitoring of REREM was conducted during 30 min observation period $^*P < 0.01$ versus sham treatment, $n = 6$, Dunnett's test

Relative electrical resistance of endothelial monolayer response to challenge with [Fe^{2+}]. Assessment of cell relative electrical resistance was used for estimation of effect of [Fe^{2+}] on the barrier properties of RPAEC monolayer. As shown in Fig. 4, 10 min pulse with [Fe^{2+}]NTA resulted in decrease in REREM values from 28.7 ± 1.3 Ω/cm^2 (sham) to 17.2 ± 1.1 Ω/cm^2 ($P < 0.001$, $n = 6$, Dunnett's test). Replacement of [Fe^{2+}]NTA with [Fe^{2+}]HBED completely abrogated the observed barrier effect (Fig. 4). The exposure of the cells to [Fe^{2+}] complexes did not result in trypan blue uptake by the treated cells. Therefore, we have associated the observed decrease in REREM with [Fe^{2+}]-induced remodeling of RPAEC monolayer. The next set of experiments focused on image analysis of the cell response to challenge with [Fe^{2+}] complexes.

Time-lapse imaging of RPAEC exposed to [Fe^{2+}] complexes. To test a potential role of structural rearrangements in RPAEC in response to challenge with [Fe^{2+}] we applied DIC (Nomarski) time-lapse imaging of confluent and non-confluent cell layers. As shown in Fig. 5, 10 min pulse with [Fe^{2+}]NTA caused contraction of the cells in confluent monolayers that was manifested by relocation of cytoplasm from peripheral to central (nuclear) sites, decrease of basolateral surface of the cells, and formation of pores

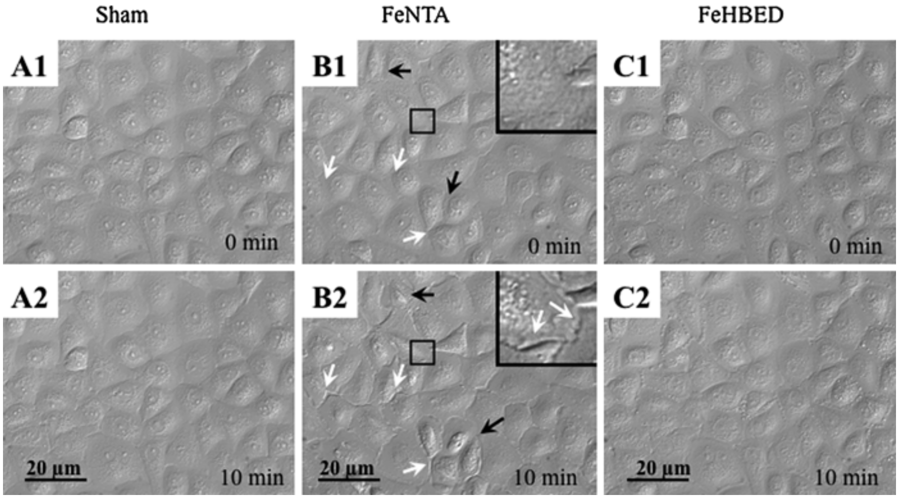

Fig. 5 Representative Nomarski images of confluent RPAEC acquired at time-frames 0 min (1) and 10 min (2) of time-lapse imaging following treatments. Panels "A1" and "A2" are sham treatments; panels "B1" and "B2" are treatments with [Fe^{2+}]NTA; and panels "C1" and "C2" are treatments with [Fe^{2+}]HBED. Alterations in cell shape (*black arrows*) and cell–cell interactions (*white arrows*) are indicated in B1 and B2. Insets are magnified selected areas indicated with *black rectangles*. *Bars* indicate 10 μm *scales*

between cell edges. The cell buckling due to [Fe^{2+}] effect was accompanied by increase in the average cell thickness up to 4.5 ± 1.5 μm (vs. 2.0 ± 0.5 μm in sham-treated cells, $n = 20$, $P < 0.02$ t test) that was assessed by spatial location of F-actin and ICAM-1 proteins in the respective confocal z-projections (see below). The iron-induced cell contraction and motility were more evident in the non-confluent cell culture where the cells had more xy-degree of freedom (Fig. 6A, B). Theabove effects were prevented when [Fe^{2+}]NTA was replaced with [Fe^{2+}]HBED (HBED is a strong [Fe^{2+}] chelator and antioxidant) in the experimental media (Figs. 6C and 5C) or with NTA alone (not shown).

Remodeling of endothelial monolayer is often accompanied by increase in their permeability to macromolecules and inflammatory cells that require a complex spatial re-arrangement of structural proteins such as F-actin and caveolin-1 (Birukova et al. 2009; Carman and Springer 2004; Chamaraux et al. 2008; Feng et al. 2002; Mehta and Malik 2006; Millán et al. 2006; van Buul et al. 2007;). Therefore, in the next set of experiments we assessed the iron-induced effects using confocal immunofluorescence image analysis.

Confocal immunofluorescence imaging of iron-induced spatial re-arragements of F-actin and pho-caveolin-1 in RPAEC. As shown in Fig. 7A1–A7 incubation of RPAEC with [Fe^{2+}]NTA resulted in spatial re-arrangement of F-actin and activated *pho*-caveolin-1 (compare to sham-treated cells, Fig. 7B). Thus, the [Fe^{2+}]NTA treated cells were characterized by increase in immunoreactivity of proteins at the central site of the cells as shown in apical and basolateral projections (A1–A6) and in ZX optical cross-section (A7). A formation of distinguishable cuplike structures abundant with F-actin and activated *pho*-caveolin-1 was observed in apical membrane rafts (Fig. 7A1, A3, A5). The iron-induced cell contraction was corroborated with Z-elevation of F-actin projections at the apical (top) regions up to 4.5 ± 1.5 μm from basolateral plane (vs. 2.0 ± 0.5 μm in sham-treated cells, $n = 20$, $P < 0.02$ t test). The spatial re-arrangement of F-actin was also accompanied by formation of microvilli-like structures in RPAECs that was revealed by ZX optical re-slicing of the collected stacks of XY projections of F-actin and *pho*-caveolin-1 (Fig. 7A7). F-actin was spatially co-localized with *pho*-caveolin-1; estimated apical spatial correlation of signals in green and red channels was $r = 0.81$. The observed cuplike and microvilli-like formations in the cells were similar to those recently described by Barreiro et al. (2002) Carman and Springer (2004); Millán et al. (2006); van Buul et al. (2007), Birukova et al. (2009). Based on observations of these and other authors the formation of the

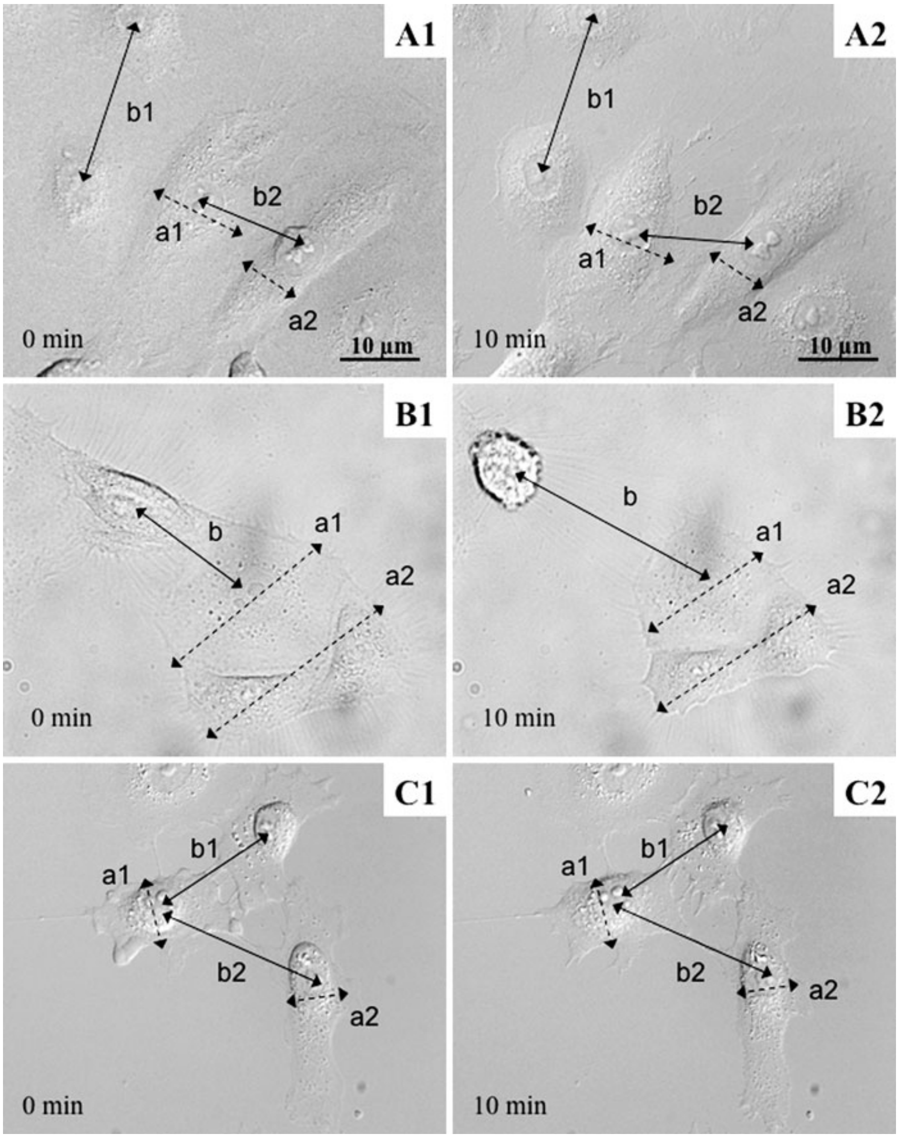

Fig. 6 Representative Nomarski images of non-confuent RPAEC acquired at time-frames 0 min (1) and 10 min (2) of time-lapse imaging following treatments. "A1" and "A2" are sham treatments; "B1" and "B2" are treatments with [Fe^{2+}]NTA; and "C1" and "C2" are treatments with [Fe^{2+}]HBED. Cell width is indicated with *dashed-line arrows* (a1 and a2); distance between the cell centers is indicated with *solid-line arrows* (b1 and b2). Note there is relative decree in a1 and a2 values in B2 versus a1 and a2 values in B1. Vice verse, there is increase in b value in B2 versus the same parameter in B1. There were no such alteration in the parameters "a" and "b" in "A" and "C"

endothelial membrane cups and microvilli-like structures mediated by cytoskeleton, caveolin-1, and ICAM-1 adhesion molecules has been proposed to be crucial in arrest of leukocytes and their migration through individual endothelial cell (EC) (Dejana 2006). Taking into consideration this concept we further assessed iron-induced effect on spatial arrangement of ICAM-1 adhesion molecules.

Confocal immunofluorescence imaging of iron-induced re-arragements of ICAM-1 and pho-caveolin-1 in RPAEC. The results of confocal image analysis of spatial arrangement of ICAM-1 and caveolin-1 proteins in RPAECs treated with [Fe^{2+}]NTA complexes are shown in Fig. 8A1–A7. The effect was characterized by increase in immunoreactivity of the proteins at the central site of the cells

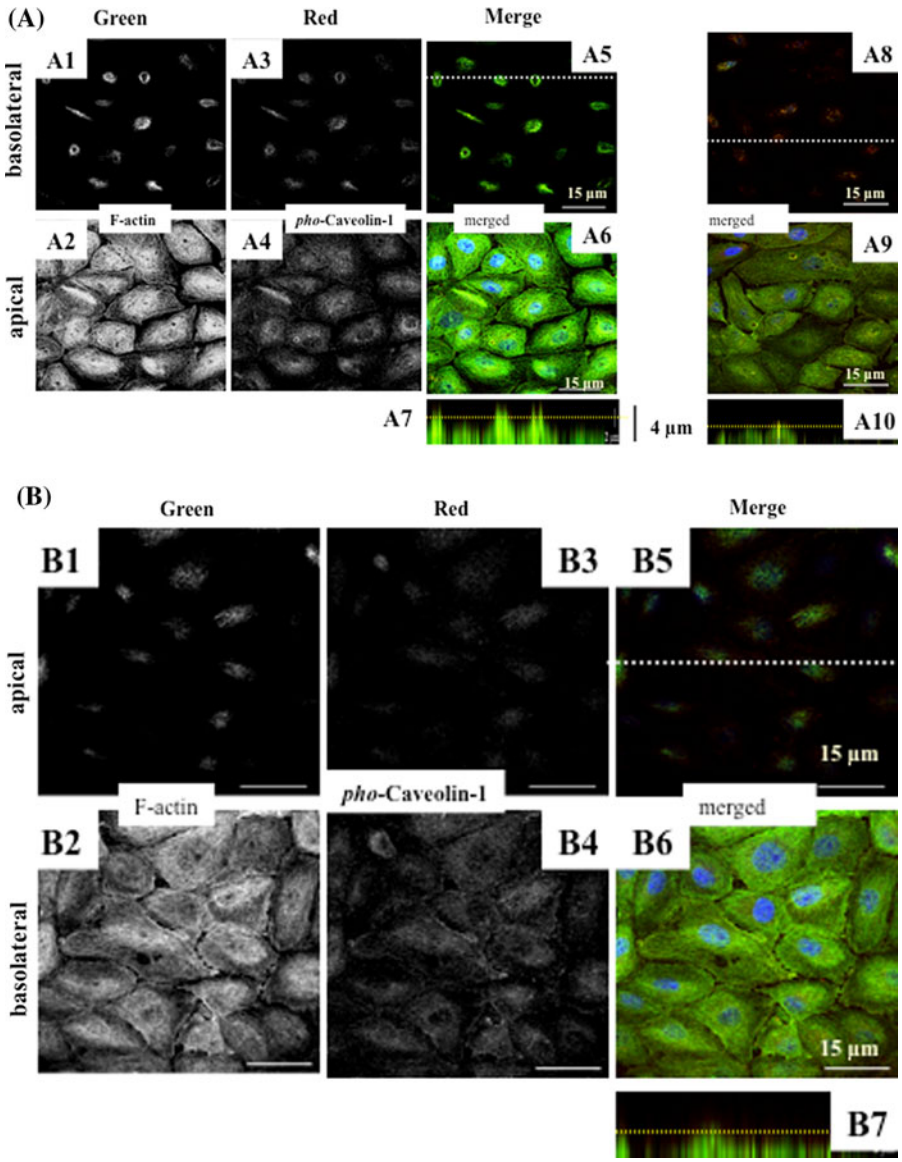

Fig. 7 Immunofluorescence confocal imaging of spatial rearrangement of F-actin and phosphorylated Caveolin-1 in RPAEC. **A** Challenge with iron complexes: A1–A7 are 10 min pulse with [Fe^{2+}]NTA and A8–A10 are 10 min pulse with [Fe^{2+}]NTA and HBED chelator. **B** Sham treatment (B1–B7). XY optical cross-sections (0.5 µm z-resolution) are shown at basolateral and apical planes. Elevation of apical XY cross-sections above basolateral planes for each set of data, i.e., A1–A7; A8–A10; and B1–B7, is indicated with *yellow lines* in the respective panel A7 (3 µm z step), A10 (2 µm z-step), and B7 (1.5 µm z-step) which represent reconstructed ZX optical cross-sections obtained by ZX-reslicing of the respective confocal Z-stacks of 10 XY images. Y-coordinates of the reconstructed ZX cross-sections are indicated with white dashed lines in panels A5, A8, and B5. Projections of F-actin (*green channel*) are shown in panels A1 and B1 (apical plane) and in panels A2 and B2 (basolateral plane). Projections of *pho*-caveolin-1 (*red channel*) are shown in panels A3 and B3 (apical plane) and in panels A4 and B4 (basolateral plane). Superposition of *green*, *red*, and *blue* (counterstaining with Hoechst 33342) projections are shown in (i) panels A5, A8, and B5 (apical plane), and (ii) panels A6, A9, and B6 (basolateral plane), and (iii) panels A7, A10, and B7 which are reconstructed ZX optical cross-sections as indicated in panels A5, A8, and B5 respectively. Co-localization of F-actin and *pho*-caveolin-1 appears in *yellow color* due to interference of *green* and *red colors*. As shown in the panels B2, B4, B6, B7 spatial rearrangements of F-actin and *pho*-caveolin-1 following exposure to [Fe^{2+}]NTA was accompanied by formation of microvilli-like projections abundant with F-actin and partially with *pho*-caveolin-1. The presented data are representative images acquired using 5 cell specimens in each group

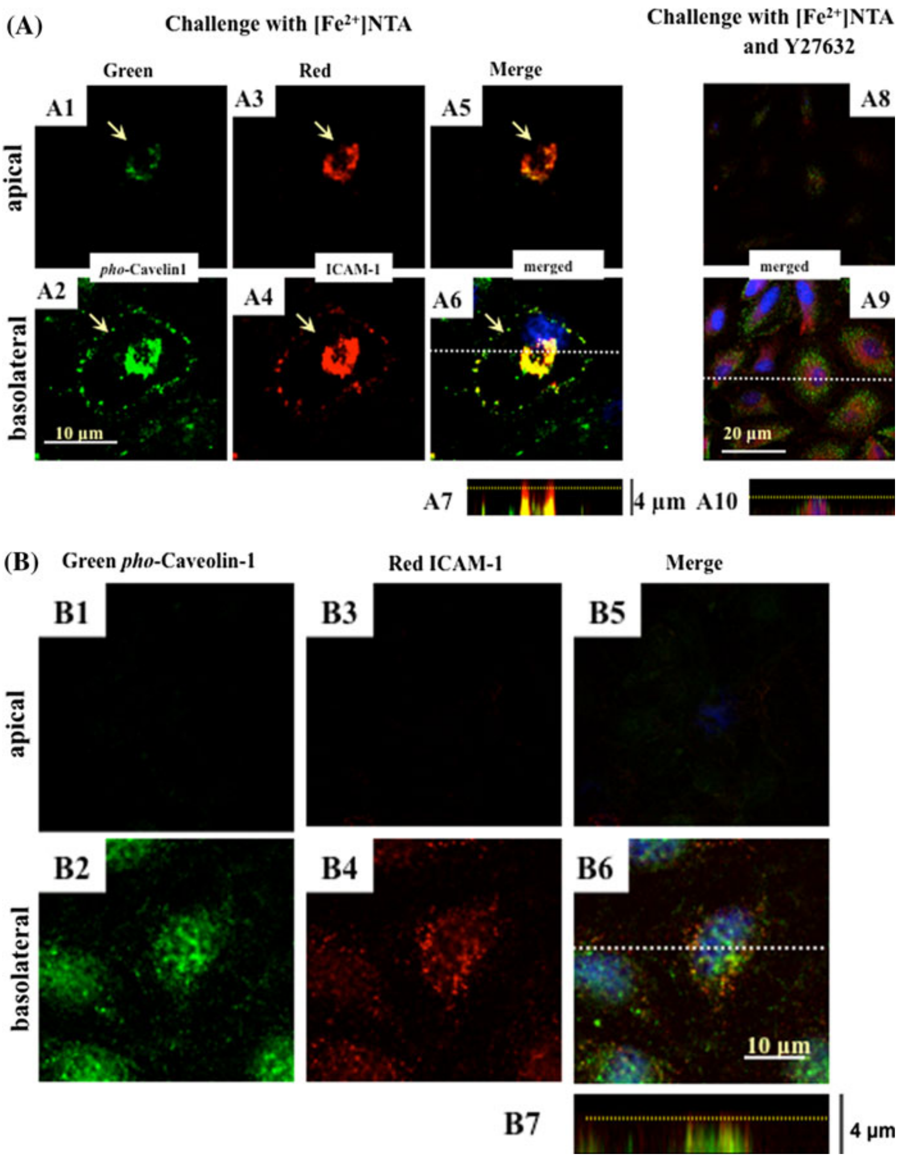

Fig. 8 Immunofluorescence confocal imaging of spatial rearrangement of ICAM-1 and *pho*-caveolin-1 in RPAEC. Challenge with iron complexes: A1–A7 are 10 min pulse with 30 µM [Fe^{2+}]NTA and A8–A10 are 30 min pre-incubation with Y27632 followed by 10 min pulse with 30 µM [Fe^{2+}]NTA. Sham treatment (B1–B7). XY optical cross-sections (0.5 µm z-resolution) are shown at basolateral and apical planes. Elevation of apical XY cross-sections above basolateral planes for each set of data, i.e., A1–A7; A8–A10; and B1–B7, is indicated with *yellow lines* in the respective panels A7 (3.5 µm z-step), A10 (2 µm z-step), and B7 (2.5 µm z-step) which represent reconstructed ZX optical cross-sections obtained by ZX- reslicing of the respective confocal Z-stacks of 10 XY images. Y-coordinates of the reconstructed ZX cross-sections are indicated with white dashed lines in panels A5, A8, and B5. Projections of *pho*-caveolin-1(*green channel*) are shown in panels A1 and B1 (apical plane) and in panels A2 and B2 (basolateral plane). Projections of ICAM-1 (*red channel*) are shown in panels A3 and B3 (apical plane) and in panels A4 and B4 (basolateral plane). Superposition of *green*, *red*, and *blue* (counterstaining with Hoechst 33342) projections are shown in (i) panels A5, A8, and B5 (apical plane), and (ii) panels A6, A9, and B6 (basolateral plane), and (iii) panels A7, A10, and B7 which are reconstructed ZX optical cross-sections as indicated in panels A5, A8, and B5 respectively. Co-localization of ICAM-1 and *pho*-caveolin-1 appears in *yellow color* due to interference of *red* and *green colors*. As shown in the panels B2, B4, B6, B7 spatial re-arrangements of ICAM-1 and *pho*-caveolin-1 following exposure to [Fe^{2+}]NTA was accompanied by formation of microvilli-like projections abundant with ICAM-1 and *pho*-caveolin-1. The presented data are representative images acquired using 5 cell specimens in each group

as appears in the apical and basolateral projections (A1–A6) and ZX optical cross-section (A7). These ICAM-1 and caveolin-1 rearrangements were in accord with those involved in F-actin and presented in Fig. 7A. Three dimensional confocal image analysis indicated that [Fe^{2+}] influx triggered structural remodeling that resulted in formation of cuplike and microvilli-like structures abundant with ICAM-1 and *pho*-caveolin-1 in the [Fe^{2+}]NTA treated cells (Fig. 9). These alterations were not observed in control cells (Fig. 8) and the cells treated with [Fe^{2+}]HBED treatment (not shown).

The observed arrangement of cuplike and microvilli-like structures was unlikely associated with p38 MAP kinase pathway since incubation of the cells with [Fe^{2+}]NTA resulted in inhibition of phosphorylation of p38 protein (not shown). However, the formation of the cuplike structures was partially eliminated by preincubation of the cells with Y27632 (panels 8 A8–7 A10) suggesting involvement of Rho-kinase in the observed structural alteration.

Based on above observations we suggest that, [Fe^{2+}]-induced re-arrangements in RPAECs can be a mechanism of pro-inflammatory remodeling where cytoskeleton and caveolin provide structural support for cell polarization and expression of proinflammatory adhesion molecules as presented in Fig. 9.

Discussion

Endothelial remodeling and an increase in vascular permeability are common features of major trauma, resuscitation, and blood transfusion and they contribute significantly to ALI and multiple organ failure syndrome (Ozment and Turi 2009; Hod et al. 2010).

These events are associated with sequential multistep alterations in EC resulting in an increase in transendothelial trafficking of biomolecules, ions, and circulatory leukocytes (Adamson et al. 2002; Gratton et al. 2004; Mehta and Malik 2006). The cellular and molecular basis of such extravasation remains unclear but it has been recently postulated that transcellular movement of blood born phagocytes via newly arranged EC pores may coexist along with the well established pathway of paracellular migration of leukocytes across transient and/or temporarily altered EC barrier function (Carman and Springer 2004; Millán et al. 2006; Dejana 2006).

We have recently shown that trauma-induced proinflammatory alterations in the lung are characterized by promotion of oxidative stress, increase in microvascular permeability and leukocyte transendothelial migration (Gorbunov et al. 2007). These effects are accompanied, by down-regulation of EC adhesion junctions and up-regulation of EC ICAM-1 adhesion molecules and are in part mediated by turnover of

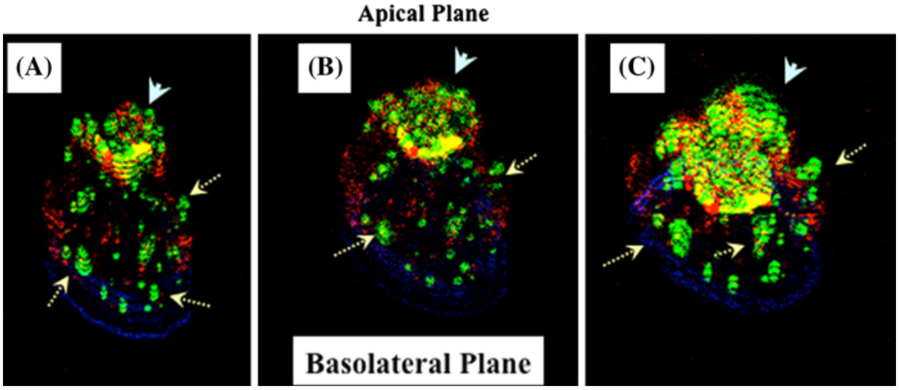

Fig. 9 3D projections of caveolin-1 and ICAM-1 in RPAEC challenged with [Fe^{2+}]NTA. Immunofluorescence of caveolin-1 is presented in *green channel*; immunofluorescence of ICAM-1 is presented in red channel. *Blue* is counterstaining of nuclei with Hoechst 33342. Spatial co-localization of caveolin-1 and ICAM-1 appears in *yellow color* due to interference signal collected in *green* and *red channels*. **a**, **b**, **c**—3D image presented at different angles of rotations. 3D projection was obtained using z-stacks of confocal images of collected in *red*, *green*, and *blue channels* (z-resolution 0.5 μm). Formation of cuplike structure at apical plane of the cell is indicated with *blue arrowheads*. The presence of caveolin-rich vesicles is shown with *dashed yellow arrows*

labile iron (Gorbunov et al. 2007). In these observations the microvascular ICAM-1 molecules were polarized toward LKC counter-receptors providing maximal engulfing of LKC during transendothelial cell migration (Gorbunov et al. 2007). The observed spatial re-arrangements of ICAM-1 were similar to those induced by pro-inflammatory stimuli in endothelium and documented by Barreiro et al. (2002) and Carman and Springer (2004), van Buul et al. (2007) who have also emphasized a crucial role of ICAM-1 polarization and formation of the cuplike structures in transendothelial cell migration. A potential role of labile iron in mediating these events remained unclear and hence the current RPAEC model was used to simulate iron-dependent pro-inflammatory effects in lung vasculature.

Herein we presented new insights into remodeling induced by redox reactive iron in vascular endothelium. We demonstrated that 10 min pulse with [Fe^{2+}]NTA in RPAEC cultures resulted in (i) redox stress-response (Fig. 2, 3), (ii) cell buckling due to contraction of cytoskeleton in basolateral plane (Figs. 5, 6, 9), (iii) decrease in electrical resistance of endothelial monolayer due to alterations in focal cell–cell interaction (Fig. 4), and (iv) cell polarization toward apical plane due to re-arrangement of cytoskeleton, caveolin-1, and ICAM-1 (Figs. 7, 8). The alterations were accompanied by formation of cuplike structures at the cell apical domains and transcellular micrivilli-like projections abundant with F-actin, caveolin-1, and ICAM-1. Similar effects were recently demonstrated in vascular EC co-cultured with LKC and/or inflammatory cytokines where they were defined being a part of pro-inflammatory remodeling essential for "docking" and the trans-cellular migration of leukocytes (Barreiro et al. 2002; Carman and Springer, 2004; Usatyuk et al. 2006).

The known transporters for NTBI and labile iron are DMT1 and SLC39A14 (or zip14). When this extracellular pool of iron is comprised by [Fe^{2+}]/[Fe^{3+}] complexes present in redox equilibrium with fluid electron donors (reductants) and electron acceptors (oxidants), absorption of [Fe^{3+}] by divalent metal transporters requires conversion of [Fe^{3+}] to [Fe^{2+}] at the surface of the cell by [Fe^{3+}] reductases (Løvstad 1995; Lane and Lawen 2008). In particular circumstances when fluid oxygenation and ferroxidase activity are suppressed, [Fe^{3+}] pool can be decreased (while [Fe^{2+}] pool-increased) by fluid reductants (e.g., ascorbate, thiols and nitric oxide). We reported relevance of such conditions to the iron redox status in pathophysiology of trauma (Atkins et al. 2006; Dubick et al. 2010; Atkins et al. 2011). Nonetheless, regardless of the route of [Fe^{2+}] formation, the absorption of NTBI results in an increased cellular load of ferrous iron.

In spite of the presence of extensive data on vascular effects of catalytically reactive iron, to our best knowledge, the present data are the first demonstration of iron-dependent endothelial remodeling similar to those initiated by LKC–EC interaction (Barreiro et al. 2002). Such remodeling likely occurred in redox dependent manner since the effect of catalytically reactive iron complexes, i.e., [Fe^{2+}]NTA, was moderated in the presence of HBED, a strong iron chelator and antioxidant, and in the presence of Y27632, a redox sensitive rho-kinase inhibitor. This suggestion is consistent with the significant effect of redox stress on cytoskeleton and endothelial permeability (Moldovan et al. 2000; Usatyuk et al. 2006). Indeed, endothelial integrity is regulated by shifting the balance between barrier-disruptive contractile forces, imposed by actomyosin filaments and barrier-protective tethering forces, imposed mainly by peripheral actin cytoskeleton, microtubules, intermediate filaments, and cell contact protein complexes (Birukova et al. 2009). The interplay between actin and the microtubule cytoskeleton is involved in the maintenance of vascular barrier, EC contractility, and cell motility (Usatyuk et al. 2006; Birukova et al. 2009). Redox stress can either directly affect microtubule assembly or it can act via focal kinase and rho-kinase (Adamson et al. 2002; Usatyuk et al. 2006). Activation of these kinases following microtubule disassembly or oxidative stress is known to promote formation of actin stress fibers and paracellular gaps, contraction of actinomyosin, formation of apical cuplike structures and dysfunction of EC barrier (van Buul et al. 2007; Birukova et al. 2009).

The current study employed a simple model system (RPAEC) and single pulse of relatively high concentrations of reduced iron (30 μM) complexed to nitriloacetate in the presence of pyrithione, an iron ionophore. This had the desired effect of acutely increasing intracellular labile pool of iron and facilitated the conclusion that such an increase was sufficient to produce the metabolic and molecular changes in RPAEC consistent with decreased barrier function and a pro-inflammatory phenotype. Nonetheless, limitations are apparent in comparing these in vitro results with pulmonary vascular changes that may occur in situ due to alterations in NTBI including the: a) nature of the iron species present in NTBI; b) relevant concentration of circulating NTBI; c) use of an ionophore and; d) non-specific effects on EC function secondary to cell death (necrosis or apoptosis). In this regard,

a) The NTBI pool is comprised of both ferrous [Fe^{2+}] and ferric [Fe^{3+}] iron complexes that are present in redox equilibrium (Cabantchik et al. 2005; Esposito et al. 2003; Turi et al. 2004; Gorbunov et al. 2006). The [Fe^{2+}]/[Fe^{3+}] redox steady state is controlled by fluid reductants (e.g., ascorbate and nitric oxide), ferroxidases and oxygen and therefore, can be shifted toward [Fe^{2+}] formation under hypoxia, ischemia, and acute hemorrhage when oxygenation and ferroxidase activity are suppressed (Atkins et al. 2006; Dubick et al. 2010; Atkins et al. 2011). Even under less extreme pathophophysiologic conditions, NTBI [Fe^{3+}] iron complexes can be converted to [Fe^{2+}] at the cell surface by localized reactions facilitated by ascorbate and/or the plasma membrane ferrireductase(s) and accordingly our use of reduced iron in model system appears justified.
b) A survey of reported high levels (~9–12 μM) of NTBI measured in various fashion in plasma of patients with thalassaemia (al-Refaie et al. 1992; Porter et al. 1996; Kartikasari et al. 2006) after iron overload (Esposito et al. 2003; Dresow et al. 2008) suggests that our use of 30 μM [Fe^{2+}] nitriloacetate was more like the unusual case of 29 μM NTBI measured in patients after cytotoxic chemotherapy (Harrison et al. 1994). Accordingly, the in vivo and clinical relevance of our observations remains to be assessed under more moderating conditions and in more complex models.
c) In the present study we have circumvented the transport mechanisms by presenting ferrous iron to the cells with an [Fe^{2+}] ionophore (pyrithione). The abrupt increase in intracellular iron (Fig. 1) provided more confidence that the induced changes were specific to the increase in iron. However there are potential limitations to this approach including: 1) the increase in intracellular iron may be larger or faster than can be accomplished by the normal transport mechanisms; 2) there is the possibility the transporter(s) for NTBI may be linked to a chaperone system that targets absorbed NTBI directly to the mitochondria (Shvartsman et al. 2007); and 3) other intercellular chaperone molecules could influence the changes in intracellular labile iron (Richardson et al. 2010).
d) Although the use of a reactive iron complex not normally found in plasma ([Fe^{2+}] nitriloacetate) may have been toxic independent of iron mediated effects, this seems less likely as there was no evidence of cell death by either trypan blue incorporation (necrosis) or TUNEL or Annexin V staining (apoptosis). Furthermore, the cytoskeleton was not disrupted but actually organized in a very specific metabolically active pattern resembling that seen after interaction of endothelium with neutrophils (Barreiro et al. 2002).

Overall, our observations indicate that the ferrous iron-induced rearrangements in the EC can be a part of a mechanism of the pro-inflammatory remodeling mediated by redox-dependent signaling. We suggest that this effect can contribute to a mechanism of pulmonary vascular inflammation that commonly occurs under acute pathophysiological conditions (trauma, blood transfusion) characterized by increase in plasma levels of chelatable NTBI.

Acknowledgments The authors thank Dr. Yulia Y Tyurina, and Dr.Valerian E Kagan for their help with assessment of cell glutathione and Mr. Geoff Daniels (Leica Microsystems Inc.) for the confocal imaging consulting. This study was supported by the Department of the Army Peer Reviewed Medical Research Program (Grant No. PR033201 to J L A.), by the US Army Medical Research and Materiel Command and R37 NIH HL65697 (B R P.).

Conflict of interest There are no ethical and financial conflicts in the presented work.

References

Adamson RH, Curry FE, Adamson G, Liu B, Jiang Y, Aktories K, Barth H, Daigeler A, Golenhofen N, Ness W, Drenckhahn D (2002) Rho and Rho kinase modulation of barrier properties: cultured endothelial cells and intact microvessels of rats and mice. J Physiol 539(Pt 1):295–308

Al-Refaie FN, Wickens DG, Wonke B, Kontoghiorghes GJ, Hoffbrand AV (1992) Serum non-transferrin bound iron in beta thalassaemia major patients treated with desferroxamine. Br J Haematol 82:431–436

Atkins JL, Day BW, Handrigan MT, Zhang Z, Pamnani MB, Gorbunov NV (2006) Brisk production of nitric oxide and associated formation of S-nitrosothiols in early hemorrhage. J Appl Physiol 100(4):1267–1277

Atkins JL, Gorbunov NV, Trabosh V, Van Dauyne R, Kashanchi F, Komarov AM (2011) Ferrous iron is found in mesenteric lymph bound to TIMP-2 following hemorrhage/resuscitation. Biometals 24:279–289

Barreiro O, Yanez-Mo M, Serrador JM, Montoya MC, Vicente-Manzanares M, Tejedor R, Furthmayr H, Sanchez-Madrid F (2002) Dynamic interaction of VCAM-1 and ICAM-1 with moesin and ezrin in a novel endothelial docking structure for adherent leukocytes. J Cell Biol 157(7):1233–1245

Birukova AA, Arce FT, Moldobaeva N, Dudek SM, Garcia JG, Lal R, Birukov KG (2009) Endothelial permeability is controlled by spatially defined cytoskeletal mechanics: atomic force microscopy force mapping of pulmonary endothelial monolayer. Nanomedicine 5(1):30–41

Cabantchik ZL, Breuer W, Zanninelli G, Cianciulli P (2005) LPI labile plasma iron in iron overload. Best Pract Res Clin Haematol 18(2):277–287

Carman CV, Springer TA (2004) A transmigratory cup in leukocyte diapedesis both through individual vascular endothelial cells and between them. J Cell Biol 167(2):377–388

Chamaraux F, Ali O, Keller S, Bruckert F, Fourcade B (2008) Physical model for membrane protrusions during spreading. Phys Biol 5(3):36009

Dejana E (2006) The transcellular railway: insights into leukocyte diapedesis. Nat Cell Biol 8(2):105–107

Dresow B, Petersen D, Fischer R, Nielsen P (2008) Non-transferrin bound iron in plasma following administration of oral iron drugs. Biometals 21:273–276

Dubick MA, Park MS, Barr JL, Atkins JL (2010) Ceruloplasmin oxidase (CPO) activity in plasma from burn and non-burn trauma patients. Inflamm Res 59:S125

Esposito BP, Breuer W, Sirankapracha P, Pootrakul P, Hershko C, Cabantchik ZI (2003) Labile plasma iron in iron overload: redox activity and susceptibility to chelation. Blood 102:2670–2677

Feng D, Nagy JA, Dvorak HF, Dvorak AM (2002) Ultrastructural studies define soluble macromolecular, particulate, and cellular transendothelial cell pathways in venules, lymphatic vessels, and tumor-associated microvessels in man and animals. Microsc Res Tech 57(5):289–326

Gorbunov NV, Asher LV, Ayyagari V, Atkins JL (2006) Inflammatory leukocytes and iron turnover in experimental hemorrhagic lung trauma. Exp Mol Pathol 80(1):11–25

Gorbunov NV, Das DK, Goswami SK, Gurusamy N, Atkins JL (2006) Nitric Oxide (NO), Redox Signaling, and pulmonary inflammation in a model of polytrauma. In: Medimond S.r.l (ed) Proceeding of the XIII congress of the society for free radical research international, Davos (Switzerland). Bologna, Italy, pp 139–144

Gorbunov NV, Das DK, Goswami SK, Gurusamy N, Atkins JL (2007) Spatial coordination of cell-adhesion molecules and redox cycling of iron in the microvascular inflammatory response to pulmonary injury. Antioxid Redox Signal 9(4):483–495

Gratton JP, Bernatchez P, Sessa WC (2004) Caveolae and caveolins in the cardiovascular system. Circ Res 94(11):1408–1417

Harada N, Kanayama M, Maruyama A, Yoshida A, Tazumi K, Hosoya T, Mimura J, Toki T, Maher JM, Yamamoto M, Itoh K (2011) Nrf2 regulates ferroportin 1-mediated iron efflux and counteracts lipopolysaccharide-induced ferroportin 1 mRNA suppression in macrophages. Arch Biochem Biophys 508(1):101–109

Harrison P, Marwah SS, Hughes RT, Bareford D (1994) Non-transferrin bound iron and neutropenia after cytotoxic chemotherapy. J Clin Pathol 47:350–352

Hod EA, Zhang N, Sokol SA, Wojczyk BS, Francis RO, Ansaldi D, Francis KP, Della-Latta P, Whittier S, Sheth S, Hendrickson JE, Zimring JC, Brittenham GM, Spitalnik SL (2010) Transfusion of red blood cells after prolonged storage produces harmful effects that are mediated by iron and inflammation. Blood 115(21):4284–4292

Kartikasari AE, Georgiou NA, Visseren FL, van Kats-Renaud H, van Asbeck BS, Marx JJ (2006) Endothelial activation and induction of monocyte adhesion by non-transferrin-bound iron present in human sera. FASEB J 20(2):353–355

Kobayashi A, Kang MI, Watai Y, Tong KI, Shibata T, Uchida K, Yamamoto M (2006) Oxidative and electrophilic stresses activate Nrf2 through inhibition of ubiquitination activity of Keap1. Mol Cell Biol 26(1):221–229

Kress GJ, Dineley KE, Reynolds IJ (2002) The relationship between intracellular free iron and cell injury in cultured neurons, astrocytes, and oligodendrocytes. J Neurosci 22(14):5848–55

Lagan AL, Melley DD, Evans TW, Quinlan GJ (2008) Pathogenesis of the systemic inflammatory syndrome and acute lung injury: role of iron mobilization and decompartmentalization. Am J Physiol Lung Cell Mol Physiol 294:L161–L174

Lane DJ, Lawen A (2008) Transplasma membrane electron transport comes in two flavors. Biofactors 34(3):191–200

Løvstad RA (1995) A kinetic study of the coupled iron-ceruloplasmin catalyzed oxidation of ascorbate in the presence of albumin. Biometals 8(4):328–331

Mehta D, Malik AB (2006) Signaling mechanisms regulating endothelial permeability. Physiol Rev 86(1):279–367

Millán J, Hewlett L, Glyn M, Toomre D, Clark P, Ridley AJ (2006) Lymphocyte transcellular migration occurs through recruitment of endothelial ICAM-1 to caveola- and F-actin-rich domains. Nat Cell Biol 8(2):113–123

Moldovan L, Moldovan NI, Sohn RH, Parikh SA, Goldschmidt-Clermont PJ (2000) Redox changes of cultured endothelial cells and actin dynamics. Circ Res 86(5):549–557

Ozment CP, Turi JL (2009) Iron overload following red blood cell transfusion and its impact on disease severity. Biochim Biophys Acta 1790(7):694–701

Porter JB, Abeysinghe RD, Marshall L, Hider RC, Singh S (1996) Kinetics of removal and reappearance of non-transferrin bound plasma iron with deferoxamine therapy. Blood 88:705–713

Quadri SK, Bhattacharjee M, Parthasarathi K, Tanita T, Bhattacharya J (2003) Endothelial barrier strengthening by activation of focal adhesion kinase. J Biol Chem 278(15):13342–13349

Richardson DR, Lane DJ, Becker EM, Huang ML, Whitnall M, Rahmanto YS, Sheftel AD, Ponka P (2010) Mitochondrial iron trafficking and the integration of iron metabolism between the mitochondrion and cytosol. Proc Natl Acad Sci USA 107(24):10775–10782

Scheiber-Mojdehkar B, Lutzky B, Schaufler R, Sturm B, Goldenberg H (2004) Non-transferrin-bound iron in the serum of hemodialysis patients who receive ferric saccharate: no correlation to peroxide generation. J Am Soc Nephrol 15(6):1648–1655

Shvartsman M, Kikkeri R, Shanzer A, Cabantchik ZI (2007) Non-transferrin-bound iron reaches mitochondria by a chelator-inaccessible mechanism: biological and clinical implications. Am J Physiol Cell Physiol 293(4):C1383–C1394

Shvedova AA, Kommineni C, Jeffries BA, Castranova V, Tyurina YY, Tyurin VA, Serbinova EA, Fabisiak JP, Kagan VE (2000) Redox cycling of phenol induces oxidative stress in human epidermal keratinocytes. J Invest Dermatol 114:354–364

Turi JL, Yang F, Garrick MD, Piantadosi CA, Ghio AJ (2004) The iron cycle and oxidative stress in the lung. Free Radic Biol Med 36(7):850–857

Usatyuk PV, Parinandi NL, Natarajan V (2006) Redox regulation of 4-hydroxy-2-nonenal-mediated endothelial barrier dysfunction by focal adhesion, adherens, and tight junction proteins. J Biol Chem 281(46):35554–35566

van Buul JD, Allingham MJ, Samson T, Meller J, Boulter E, García-Mata R, Burridge K (2007) RhoG regulates endothelial apical cup assembly downstream from ICAM1 engagement and is involved in leukocyte trans-endothelial migration. J Cell Biol 178(7):1279–1293

Zhang LM, St Croix C, Cao R, Wasserloos K, Watkins SC, Stevens T, Li S, Tyurin V, Kagan VE, Pitt BR (2006) Cell-surface protein disulfide isomerase is required for transnitrosation of metallothionein by S-nitroso-albumin in intact rat pulmonary vascular endothelial cells. Exp Biol Med (Maywood) 231(9):1507–1515